Molecular Dynamics Characterization of the Water-Methane, Ethane, and Propane Gas Mixture Interfaces

Sina Mirzaeifard, Phillip Servio, Alejandro D. Rey*

Department of Chemical Engineering, McGill University, Montreal H3A 0C5, Canada

Abstract

The co-existing natural gas and water bulk phases arise in a wide range of technological and environmental processes. The liquid-gas mixture is separated by an interface which plays a crucial role in mass transport across the phases. In this work, we use the molecular dynamics (MD) technique to investigate the molecular organization, solubility, density, and compositions of natural gas-water interfaces. We apply the NP_NAT ensemble which is an appropriate statistical methodology to dodge the defects of the conventional ensembles in surface physics, and ultimately, to characterize the interfacial thermodynamics and mechanics. High interfacial density, excess, and radial pair distribution function of the gas components in order of propane, ethane, and methane, respectively, suggest the interfacial adsorption as per favorable interactions with a dense hydrogen bonding network near the surface in the liquid water phase. It is also found that the gas components solubility is negligible. Nevertheless, methane molecules present in natural gas can further dissolve in water, comparing to pure methane. We lastly conclude a heterogeneous formation of structure II hydrate from the adsorption and composition results. Moreover, we systematically increase the pressure from 1 MPa to 50 MPa and the temperature from 273.15 K to 303.15 K to calculate the interfacial tension using the mechanical approach. We observe a decrease in the interfacial tension along with an increase in both pressure and temperature. Given the remarkable hydrocarbon adsorption acting as a surfactant, this interfacial tension attenuation is more highlighted in a natural gas-water system compared to the pure liquid-vapor water or water-pure methane systems at the same temperature and pressure. We employ MD combined with fundamental thermodynamics to predict the interfacial tension via its independent relations with pressure and temperature which agrees with the classical scaling laws, namely, the Eötvös rule. The corresponding molecular mechanisms captured by the microscopic and macroscopic

properties at the interfacial regions prospectively demonstrate a sensitivity to both temperature and pressure, which contributes to the developing understanding and applications of the imperative water-natural gas interface.

Keywords: water-natural gas mixture interface; gas hydrates; surface physics; interfacial tension; molecular dynamics simulation; NP_NAT ensemble.

Introduction

The coexistence of natural gas and water is found in the oil and gas industries [1, 2] and in biological systems [3]. It also plays a significant role in terms of environmental impact [4], and has a strong relevance to climate science [5]. In all these processes and phenomena, the methane, ethane, and propane mixture, as the main constituents of the natural gas, is directly in contact with liquid water [6] and hence interfacial thermodynamics and interfacial transport phenomena at the water-natural gas (W/NG) interfaces play an important role [7]. In particular the interfacial tension governs the capillary pressure involved in the fluid dynamics in petroleum pipelines and reservoirs, which is vital for many processes such as exploration and production [8, 9]. Despite its technological and fundamental physics importance, the molecular-level understanding and characterization of W/NG interfacial properties, interfacial composition and mechanics remains incomplete.

Under frequently found natural and industrial temperature and pressure conditions, the interactions of natural gas and water molecules may trigger the nucleation of clathrate hydrates. Clathrate or gas hydrates are ice-like crystalline solids which consist of the gas, guest molecules, encapsulated inside of the metastable host water cavities [10]. Depending on the guest gas molecules, the hydrates can form different crystalline structures known as structure I [11], structure II [12, 13], and structure H [14]. Clathrate hydrates are central to many industrial applications such as flow assurance, gas storage, climate change, alternative energy resources, and transportation [15]. For instance, clathrate hydrates reserves are estimated to be able to provide up to three orders of magnitude more energy than the diminishing fossil energy reserves [1, 10], which promotes our incentives. The main motivation of this work is to characterize the interfacial energy

contribution in the nucleation process of gas hydrates by performing a molecular-level study of the natural gas-liquid water interface.

Motivation

We briefly elaborate on the motivation of this work. According to the classical nucleation theory (CNT), the hydrate formation can be categorized as either homogeneous or heterogeneous but the process remains incompletely understood [16, 17]. Elucidating the basic theory behind the clathrate formation is important in order to discover efficient methods of promoting or inhibiting their formation, depending on the above-mentioned applications. Among all the theories in crystallography, the classical nucleation theory is still the basis of the most modern nucleation studies, which can successfully describe the work of clathrate formation, namely, ice and gas hydrate [10, 18-20]. After necessary assumptions, this work is divided into two contributions including spontaneous formation of a new phase and the interfacial energy cost [21]:

$$W(J) = -n\Delta\mu + c(nv_h)^{\frac{2}{3}}\sigma \quad (1)$$

where n, $\Delta\mu(J)$, c, v_h (m^3), and σ (J/m^2) denote the number of crystal unit cells, supersaturation, shape factor, hydrate volume, and surface energy, respectively. Hence, to make progress with the understanding of this formation work, we need to calculate the interfacial energy between all the involved phases including liquid-gas, hydrate-gas, and liquid-hydrate. Fig. 1 (a) shows schematic examples of hydrate formation. Many factors such as different hydrate phase morphologies [22] and fluid flow in natural or industrial environments might affect the formation [23-25]. The interfacial boundaries between different existing phases dictate the ideal location and process for the hydrate nucleation [26]. Thus, an extensive characterization of the interfacial energy between the natural gas and liquid water phases is vitally important to hydrate science.

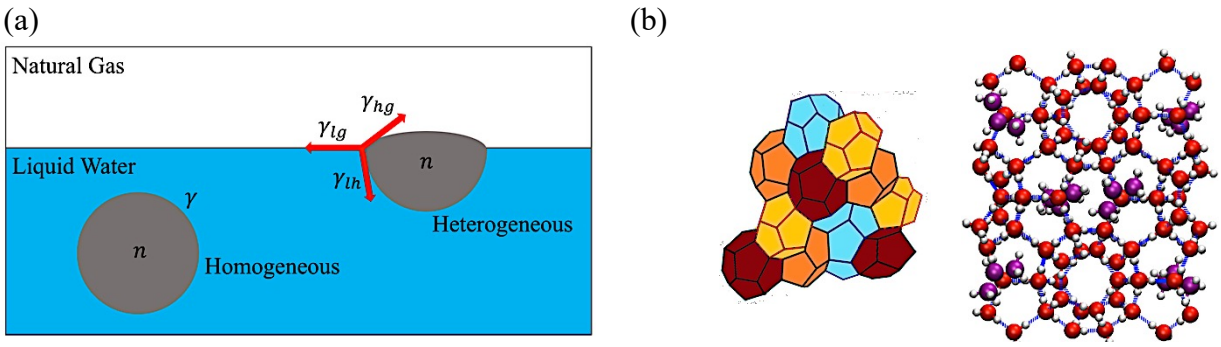

Fig. 1. (a) Introducing different clathrate formation processes. γ is the interfacial tension of the homogeneous formation of gas hydrates. γ_{lg}, γ_{hg}, and γ_{lh} denote the interfacial tension between the liquid-gas phases, the hydrate-gas phases, and the liquid-hydrate phases, respectively. In this work, we study γ_{lg} where the liquid is water. (b) Geometric configuration of structure II hydrates alongside a snapshot of propane hydrate. The purple, red, and white particles denote the propane molecules, the oxygen atoms, and the hydrogen atoms, respectively. The blue dashed lines represent the hydrogen bonding network.

In this study, we assume the surface energy is the same as the surface tension in large scale formation [27]. Therefore, to capture the interfacial energy between different phases including natural gas-liquid water, one needs a sound knowledge of the tensorial stress governing the interface mechanics. The interfacial tension between the liquid and hydrate phases to reach the total interfacial energy contribution can also be obtained using the Young equation [28], which is not within the scope of this work.

The understanding of the nature of interfacial interactions is of great importance to elucidate the thermodynamic stability, phase transitions, morphology, nucleation, and the growth rate of clathrate hydrates, which requires novel experimental techniques, theoretical modeling, or computational characterization. The molecular structure and organization at the surface predominantly influence the bulk and interfacial properties of the water-natural gas systems. Hayama *et al.* propound to investigate the effects of different alkanes on the molecular mechanism at the interface, which cannot be explained in their experiments [29]. Furthermore, Speight *et al.* state that surface tension increases with molecular weight [30] while this relation is unclear in the mixtures. Moreover, Wang *et al.* observes that mixing the gas components changes their solubility in liquid water/alcohols, which tremendously affects the mechanism of the hydrate inhibitors, but the reason is poorly understood [31]. To the best of our knowledge, this is the first work that attempts to simulate the water-natural gas mixture in order to answer all these crucial questions. Furthermore, based on the W/NG interface characterization, we deduce features of the heterogeneous nucleation of structure II hydrates, whereas the ubiquitous methane molecules in

ocean sediments insinuate that structure I hydrates would probabilistically form [15, 32, 33]. Fig. 1 (b) show a configuration sample of structure II hydrates.

Experimental characterization of the W/NG interface at conditions relevant to gas hydrate nucleation is challenging due to the high pressure for hydrate formation, need of molecular-level measurements, and sample impurities leading to inaccurate results [34, 35]. Hence, we seek insights into the microscopic interfacial regions using computer simulations, which can effectively provide all the essential information. Nonetheless, molecular simulations encounter challenges of its own at water-hydrophobic gas interfaces, explicitly, sudden local density variation, robust hydrogen bonding, ion binding, topological disturbance, discontinuity of macroscopic fields, spontaneous interfacial contraction, and sufficient time and length scales for reliable results. These issues can be appropriately overcome by applying the methods to mimic realistic models and leverage the study of the distinct thermodynamic and mechanical behaviors at the bulk and interfaces [36, 37]. In this work, we employ very powerful molecular dynamic (MD) techniques in conjunction with sophisticated interfacial thermodynamics to investigate molecular organization, weights, structure, and solubility of large alkanes. In addition, we readily calculate the crucial interfacial tension from pressure tensor analysis, and subsequently, derive classical scaling laws to characterize the complex natural gas-water interface as a function of pressure and temperature. The key aspect of our approach is to observe the molecular structures of a pure mixture with no external disturbances to further uncover the theoretical physics behind the phase co-existence at both microscopic and macroscopic levels.

Computational Challenges

We briefly comment the computational challenges in capturing the physics and thermodynamics of the W/NG interface. Some thermodynamic and physical parameters including the local density and potential energy express non-uniform behavior along the normal direction to the liquid-gas interface. We tackle this problem in surface science with the selection of a proper statistical ensemble to provide sensible results. In general, the appearance of multiple phases consisting of anisotropic interfaces constrains the choice of ensemble. The thermodynamics and mechanics of the system differ in the normal and lateral directions at the interface. Consequently, the standard *NPT* ensemble cannot guarantee reliable interfacial properties. This ensemble requires

adjusting a uniform pressure, whereas, the stress tensor loses its constancy along the simulation box so that the tangential pressure suddenly drops at the interfaces. On the other hand, the conventional *NVT* ensemble could be an alternative to automatically calibrate the pressure resolving the above-mentioned concerns. Nevertheless, this ensemble might fail because of the lack of information over the system volume. Therefore, we need to use a unique ensemble in surface studies, which is independent of complete knowledge over the system volume or the tangential pressure at the interface, and simultaneously, controlling the temperature and pressure across the mixture to avoid the disturbances in the interfacial regions. Herein, we propose to employ the NP_NAT ensemble, which only sets the constant cross-sectional area (A) and normal pressure (P_N) imposed onto the planar surface. This sophisticated ensemble has been previously used to predict the most sensible values of liquid-gas systems [38, 39], anisotropic liquid-solid interfaces [40] and polar lipid bilayers in cell membrane [41].

In modern computational physics, there are two thermodynamic and mechanical approaches to calculate the interfacial tension of mixtures [42-44]. In the thermodynamic approach, one might derive the surface tension from the change in interfacial free energy over the associated area. This definition mainly targets the global properties [45], while we intend to pursue both global and local perspectives of the system. In addition, the interfacial area must remain static in the NP_NAT ensemble throughout the simulations leaving the mechanical approach as a pragmatic option for us to effectively estimate the interfacial tension of a system with a density gradient in only one dimension. Therefore, we need to obtain the local components of the pressure tensor at the natural gas-water interface obeying the Kirkwood and Buff technique [44].

The organization of this paper is as follows. In the next section, we concisely describe the models and MD simulation including the novel method for the calculation of the liquid-gas interfacial tension. In the results and discussion section, we analyze the density, adsorption, solubility, and molecular organization at the interface. In addition, the temperature and pressure effects on the interfacial tension, structure, thickness, and entropy are discussed. Finally, we present the main conclusions of this work, and the novelty and significance of the results for current and future studies.

Model and Simulation Methods

We employ the molecular dynamics technique to investigate the classical thermodynamic behavior of the water-natural gas mixture at its interface as a function of pressure and temperature We follow the common computational method in surface science and confine the liquid water phase between two gas phases as shown in Fig. 2 (a) [44, 46]. Then we apply periodic boundary conditions for the simulation box with the initial size of 36×36×200 Å in three dimensions. The NP_NAT ensemble requires the fixed box lengths in the x and y dimensions to provide a constant cross-sectional area (i.e., $A = L_x L_y$). The initial value of the box length in the z dimension (L_z) is arbitrary as we allow the box to independently dilate or contract in that direction [47]. This procedure regulates the system volume so we can attain the desired target pressure, and consequently, the prescribed bulk density for coexisting liquid and gas phases towards equilibration. We design the simulation box with two distinct molecular configurations. In the first scenario, we randomly place 600 molecules for each individual gas component in a slab in the middle of the simulation box and surround this slab with 3825 water molecules on both sides. Hereby, we seek to better understand the effect of molecular weight and structure of the different hydrocarbons in an identical situation. Next, we form another configuration with a realistic gas composition to tailor the natural gas for the second scenario. We confine 3825 water molecules between two regions of the gas molecules, which altogether consist of 600 methane molecules, 45 ethane molecules, and 17 propane molecules following the natural gas composition from experiments [16]. Fig. 2 (b) depicts one snapshot of a typical initial configuration of this case. Fortunately, we can study the water-natural gas interfacial properties and the timely access to experimental data [29] allows us to validate the methods and predictions.

(a)

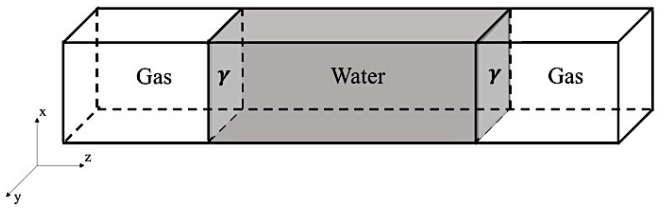

(b)

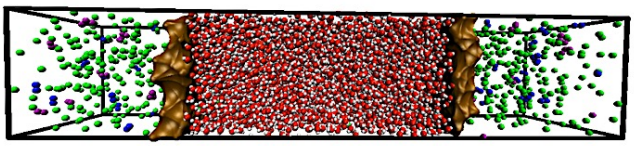

Fig. 2. (a) Schematic showing the water and gas molecules in grey and white zones to represent the liquid and gas phases, respectively. (b) Snapshot of the initial configuration of the system. The green, blue, purple, red, and white particles denote the methane molecules, the ethane molecules, the propane molecules, the oxygen atoms, and the hydrogen atoms, respectively. The brown regions define the interfaces separating the gas and liquid phases.

In the present work, we employ the transferable intermolecular potential with the four points (TIP4P) model [48] and united atom optimized potentials for liquid simulations (OPLS-UA) model [49] to simulate the force fields for water and gas molecules, respectively, within the LAMMPS simulation package [50]. To calculate the Coulombic electrostatic interactions, we apply the particle-particle particle-mesh (PPPM) technique, optimized for the TIP4P model, introduced by Hockney and Eastwood [51, 52] with an accuracy of 10^{-5} for the errors in force computation. Moreover, we utilize the Lennard-Jones (LJ) potential with Lorentz-Berthelot approach as an arithmetic mixing rule for the unlike particles to represent the intermolecular interactions:

$$U_{LJ}(r) = 4\varepsilon\left[\left(\frac{\sigma}{r}\right)^{12} - \left(\frac{\sigma}{r}\right)^{6}\right] \tag{2}$$

$$\varepsilon_{ij} = \sqrt{\varepsilon_{ii}\varepsilon_{jj}} \tag{3}$$

$$\sigma_{ij} = \frac{\sigma_{ii}+\sigma_{jj}}{2} \tag{4}$$

where ε, σ, and r denote the potential well depth, the finite distance at zero potential, and the distance between the particles, respectively. We choose the cut-off distance of 12 Å for LJ and short range electrostatic interactions. Table 1 expresses the required simulation data, including the partial electron charges, the distance and the angles between atoms or charge sites, and LJ potential parameters [48, 49]. An additional force is applied through the Shake algorithm to constrain the bonds and the angles associated with the bonded molecules including the water, the ethane, and the propane. Using such force can guarantee all bond lengths and angles remain constant throughout the simulations.

Table 1
Molecular weights, distance and angles between atoms or charge sites, partial electron charges, and Lennard-Johns potential well depth (ε) and finite distance (σ) determine the simulation parameters.

	mass (g/mol)	σ (Å)	ε (kcal/mol)	charge (e)

O	15.999	3.164	0.163	-1.0484
H	1.0080	0	0	0.5242
CH_4	16.042	3.733	0.294	0
CH_3 (ethane)	15.035	3.775	0.207	0
CH_3 (propane)	15.035	3.905	0.175	0
CH_2 (propane)	14.027	3.905	0.118	0
O-H bond length		0.9572 Å		
H-O-H angle		104.52°		
O···M distance		0.125 Å		
C-C bond length		1.526 Å		
C-C-C angle		112.4°		

The Verlet algorithm is used to integrate the non-Hamiltonian equations of motion within each time step of 2 fs. In addition, we retain the scaling of the particles velocity to control the temperature, and subsequently, to sample the system configuration using the desired ensemble. Nosé-Hoover thermostat and Parrinello-Rahman barostat couple the dynamic variables to the motion equations to regulate the temperature and the pressure with the damping constant of 4 ps for the inherent fluctuations. The simulations are carried out for 10 ns, which is sufficiently long to ascertain the thermodynamic equilibrium state. To support the practical equilibration time of 3-4 ns, we observe no major variation in the mechanical and thermodynamic properties of the system such as the pressure and the temperature, and simultaneously, the correlation factor for the potential energy rapidly vanishes. Nonetheless, we analyze the simulation outcome collected from the last 1 ns to guarantee acceptable accuracy.

The following equation is used to calculate the interfacial tension from the Kirkwood and Buff method (γ_{KB}):

$$\gamma_{KB} = \int_{-\infty}^{+\infty} \left(P_N - P_T(z)\right) dz \quad (5)$$

where P_N and P_T indicate the normal and tangential pressures, respectively. This integral is calculated over the entire simulation box in the z direction. We then compute P_N and P_T from the stress tensor [53]:

$$P_N = P_{zz} = P \tag{6}$$

$$P_T = \frac{1}{2}\left(P_{xx} + P_{yy}\right) \tag{7}$$

Ignoring the slight computational fluctuations, these normal and tangential pressures are constantly identical to the total pressure along the simulation box excluding the interfacial regions. While, the tangential pressure considerably drops at the interface producing a positive value for the difference between the normal and tangential pressures. Additionally, we use the mean values for the stress tensor components to calculate the surface tension, in an analogous manner to our previous work [54]. Please note that the integral (Eq. (5)) is divided by two, given the existence of two evolved interfaces between water and gas molecules along the simulation box. Hence, the surface tension can be obtained from:

$$\gamma_{KB} = \frac{L_Z}{2}\left[\langle P_z\rangle - \frac{1}{2}\left(\langle P_{xx}\rangle + \langle P_{yy}\rangle\right)\right] \tag{8}$$

However, the truncations in the computation process of the interatomic interactions causes the interfacial energy obtained from the mechanical definition (Eq. (8)) to be underestimated [55, 56]. The cut-off distance in the interatomic interactions weakens the interfacial tension along with the bulk pressure at a constant density. In the inhomogeneous systems such as the mixture in this study where all the phases are engaged with all the components, the drop in the interfacial tension calculation is much highlighted [57]. To compensate for the surface tension inaccuracy in multicomponent systems, we require a tail (long-range) correction given by Blokhuis *et al.* [55]:

$$\gamma_{tail} = \int_0^1 \int_{r_c}^{\infty} 12\pi\varepsilon\sigma^6\left(\rho_l - \rho_g\right)^2 \left(\frac{3s^3 - s}{r^3}\right) cot\left(\frac{rs}{d}\right) dsdr \tag{9}$$

where r_c, d, s, and ρ_l and ρ_g represent the cut-off distance, interfacial thickness, position, and molecular densities of the liquid and gas phases, respectively. Accordingly, we obtain the interfacial tension (γ) from the following equation throughout the simulations:

$$\gamma = \frac{L_Z}{2}\left[\langle P_z\rangle - \frac{1}{2}\left(\langle P_{xx}\rangle + \langle P_{yy}\rangle\right)\right] + \int_0^1 \int_{r_c}^{\infty} 12\pi\varepsilon\sigma^6\left(\rho_l - \rho_g\right)^2 \left(\frac{3s^3 - s}{r^3}\right) cot\left(\frac{rs}{d}\right) dsdr \tag{10}$$

Results and Discussion

The mass density and component concentration are the initial quantities of interest. We need to obtain a firm knowledge of the interfacial mass density profile which can later contribute in the tail correction of the interfacial tension calculation. In addition to the bulk density, we obtain the

local mass densities of all the components (i.e., water, methane, ethane, and propane molecules) to discern the molecular distribution along the simulation box.

To elucidate the effects of the different hydrocarbons, we follow the scenario one in the method section and build a system with an equal mole fraction for each of the components in the natural gas at 298.15 K and 10 MPa. Fig. 3 exhibits a peak in the density profile in the gas side near the interface owing to the compressive forces between the gas components. An accumulation of gas molecules onto the water surface might interpret the existence of this peak. This anomalous adsorption points to the heterogeneous mode of hydrate nucleation, which occurs at the interface of natural gas and liquid water. Such phenomena for solitary methane molecules in contact with water has been previously reported [54, 58]. Herein, Fig. 3 (a) depicts that the presence of the ethane molecules might change the composition of the natural gas at the interface so that the ethane molecules have priority to the methane molecules in terms of the interfacial adsorption. Likewise, Fig. 3 (b) shows that the insertion of the propane molecules with identical quantity into the gas mixture leads to the enrichment of the propane molecules followed by the ethane molecules with a negligible methane enrichment.

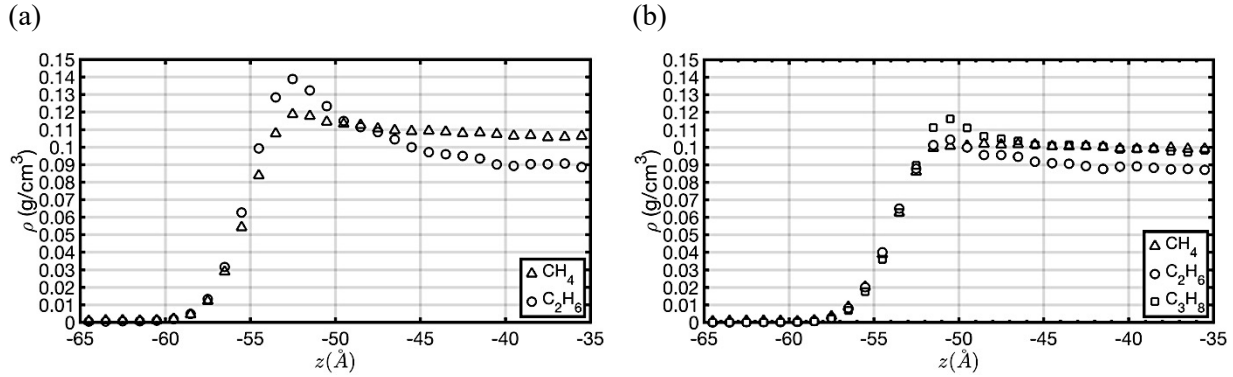

Fig. 3. Local density profiles (g/cm3) of the water-gas mixture with (a) and without (b) the propane molecules near the interface at 298.15 K and 10 MPa. The triangle, circle, and square markers denote the methane, ethane, and the propane concentrations, respectively. When the system contains large hydrocarbons, the gas adsorption onto the water surface sequentially occurs from large to small molecules. Please note that the interface center is -50 Å, which is obtained from the inflection point of fitted density profiles.

To quantify this segregation effect, we calculate the component adsorption Γ_i from the surface excess of each of the gas components:

$$\Gamma_i(\mathrm{mol}/m^2) = \frac{1}{A}\int_{-\infty}^{\infty}\{\rho_i(z) - \rho_{i,l}\Theta(-z) - \rho_{i,g}\Theta(z)\}\,dz, \quad (11)$$

where ρ_i, $\rho_{i,l}$, $\rho_{i,g}$, and $\Theta(z)$ denote the component i density profile (g/cm^3), bulk density (g/cm^3) in liquid and gas phases, and Heaviside step function, respectively. Table 2 reports the surface excess of the gas components in the systems with and without the propane molecules. We expectedly observe that the maximum surface excess is associated with the largest saturated hydrocarbons.

Table 2
Interfacial excess of the water-gas mixture with and without the propane molecules at 298.15 K and 10 MPa.

	$\Gamma_{CH_4}(10^{-6}\ \mathrm{mol}/m^2)$	$\Gamma_{C_2H_6}(10^{-6}\ \mathrm{mol}/m^2)$	$\Gamma_{C_3H_8}(10^{-6}\ \mathrm{mol}/m^2)$
CH_4+C_2H_6	2.50	3.93	-
CH_4+C_2H_{6+}+C_3H_8	2.39	2.74	2.80

To evaluate the molecular distribution in the system, we now characterize the chemical composition across the left interface. Since we encompass the gas in the central region between the water molecules, the mass fraction of the gas components prevails over the liquid water as we move from the box sides towards the center. Fig. 4 depicts the concentration profiles for the water and gas molecules along the box length in the z direction. Negligible mass fraction for the gas components in the water phase is observed. We hypothesize that the presence of a firm hydrogen bonding (HB) network among the polar water molecules near the interface restricts the mobility of nonpolar gas molecules between the phases. Nevertheless, the gas components in order of their size may escape through this hydrogen bonding network, and slightly, penetrate the water phase. This penetration is more vivid for the methane molecules as the smallest hydrocarbon in the natural gas composition. The adsorption of the ethane and propane molecules also obliges few more methane molecules to be released into the water phase. The same results for the gas components solubility have been previously observed in the experiments [31, 59]. To confirm this hypothesis, we will consider a more realistic model later in this document to analyze the interaction between the hydrogen bonding and gas molecules. In general, these obtained gas concentration results in combination with the graded adsorption from high to low hydrocarbons are the first computational predictions, which elucidates why the natural gas at the favorable thermodynamic conditions heterogeneously forms the structure type II hydrates under the classical nucleation theory classification.

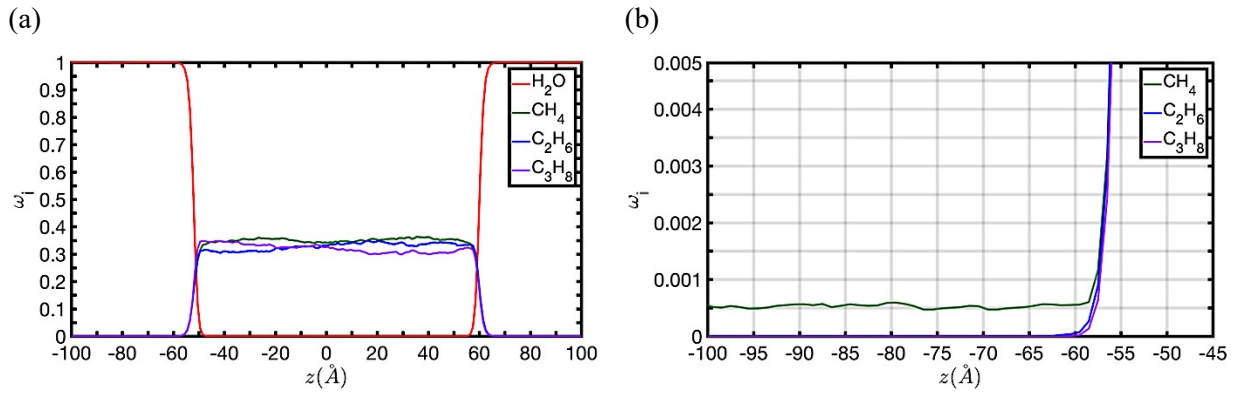

Fig. 4. The plot (a) shows the mass fractions of water (red), methane (green), ethane (blue), and propane (purple) molecules at 298.15 K and 10 MPa. The plot (b) enlarges the mass fractions of the gas molecules in the liquid phase to illustrate the minor solubility of the methane molecules and the infinitesimal penetrations of the ethane and propane molecules inside the liquid water phase. Please note that the centers of the left and right interfaces are -50 Å and 62 Å, respectively, which are obtained from the inflection points of fitted density profiles.

We now use the other example with the mass fractions close to natural gas composition to examine the graded adsorption scenario in more realistic model. In this model, the water molecules are encapsulated between the gas molecules. Fig. 5 exhibits a considerable loss in the potential energy at the interface as we move from the side gas phases to the central liquid phase in the z direction. This loss coincides with a major upturn in the water local density.

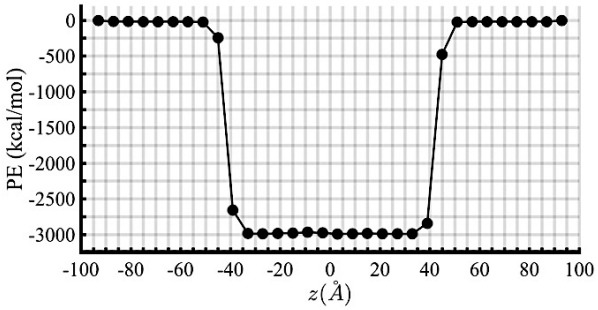

Fig. 5. Potential energy (kcal/mol) of a system at 298.15 K and 10 MPa. As the mass fraction of the gas molecules decreases, consequently, the water mass fraction increases so that the system reveals a dramatic decrease in its local potential energy.

We calculate the radial pair distribution function of the gas components and water molecules at the interface to assess the effects of large hydrocarbon on the interfacial adsorption. Fig. 6 clearly validates the previous conclusion that the water surface is covered with ordinal layers of propane, ethane, and methane molecules. The distribution functions show an initial spike at the same distance for the different components expressing the first layer of adsorption populated with more

propane molecules. However, this spike is more pronounced for the methane and ethane molecules followed by a smooth increase in their distribution functions. The propane molecules show more fluctuations owing to their longer molecular length. It is worth mentioning that the propane molecules tend to lay in parallel, as opposed to perpendicular, on the water surface as the radial pair distribution functions for the CH_2 and CH_3 groups in the propane molecules are nearly the same, analogous to the purple lines shown in Fig. 6. The results for the CH_2 and CH_3 groups are not individually shown in the figure since the differences with the propane distribution function is extremely infinitesimal. Although the methane, ethane, and propane have different molecular lengths, the adsorption trend is equivalent, which emphasizes on a parallel molecular orientation for the ethane and propane molecules.

This interfacial adsorption trend concluded from the density profile, the surface excess, and the radial pair distribution function calculations suggests the hydrate formation of structure sII, which involves the large saturated hydrocarbons. Moreover, the system at a lower temperature, which is thermodynamically more favorable for hydrate nucleation, shows an additional adsorption of the gas molecules facilitating the heterogeneous hydrate nucleation (see Fig. 6 (b)).

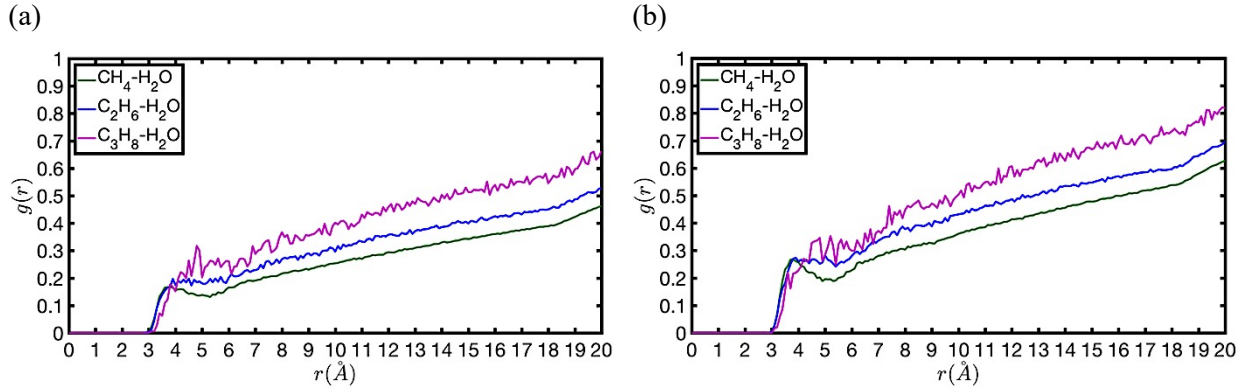

Fig. 6. Radial pair distribution functions of the system at (a) 298.15 K and (b) 275.15 K, and 10 MPa. The plots present the multilayer adsorption of gas molecules onto the water surface. The adsorption enhances once the system experiences lower temperature as shown in the plot (b).

Herein, we compute the number of hydrogen bonds between the water molecules near the interface in a system at 298.15 K. We define the hydrogen bonding criterion by $O-O$ distance and $O\cdots O-H$ angle less than 3.5 Å and 30°, respectively, and average the computed number across 1000 configurations at equilibrium. Subsequently, we remove the ethane and the propane molecules from the systems to investigate the effect of the gas components coexistence. Furthermore, we reduce the temperature to 275.15 K, which thermodynamically provides the more

favorable condition for the hydrate formation, to explore how the number of hydrogen bonds is pertinent to the system temperature. Fig. 7 (a) implies that the water molecules tend to form a denser hydrogen bonding network near the interface separating the surface water from the bulk water with distinct molecular-level organizations. Therefore, we speculate that the interfacial gas adsorption is attributed to more favorable interfacial interaction between the hydrogen bonds and the gas components in the water and the gas phases, respectively. Since the number of hydrogen bonds in a simple mixture of water and methane molecules appears to be lower than the natural gas-water system, we postulate that the number of hydrogen bonds increases with the natural gas molecular weight. On the other hand, the linear structure of ethane and propane molecules can better influence the hydrogen bonding network compared to the spherical methane molecules. Moreover, Fig. 7 (b) evidently demonstrates that the hydrogen bond density near the surface increases as the temperature decreases, which leads to more adsorption of the larger hydrocarbons on the interface allowing the heterogeneous nucleation of the structure II hydrates. Additionally, this hydrogen bond-gas interaction predominantly triggers the compressive forces on the gas components yielding poor solubility of natural gas in liquid water at T<303K and 10 MPa, which agrees with the earlier results obtained from the concentration profiles.

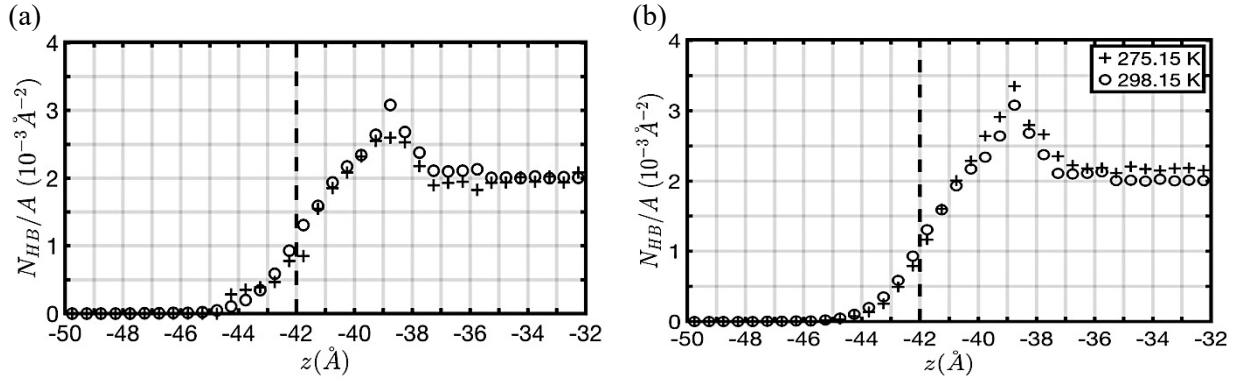

Fig. 7. The plot (a) depicts the hydrogen bond quantity at the interface. The plus sign and circle markers represent the water-methane mixture and the water-natural gas mixture, respectively. Dashed line defines the interface center obtained from the inflection point of fitted density profiles. The plot shows that the presence of large hydrocarbons consolidates the interfacial hydrogen bonding. The temperature of the system is subject to change in the plot (b) to show the hydrogen bonding network near the interface is intensified in lower temperature regimes. The plus sign and circle markers denote the temperature of 275.15 K and 298.15 K, respectively.

We can now calculate the interfacial tension between the liquid water and the natural gas phases using Eq. (10) to compare the results with the experiments and authenticate our method. In

addition, we anticipate this calculation will support the findings of hydrate formation in different thermodynamic pressure and temperature regimes.

To calculate the interfacial tension, we increase the system pressure from 1 MPa to 10 MPa at the same temperature and gas composition following the experiments [29]. The deficient interactions between the interfacial molecules in the normal direction as compared to the bulk penalize the interfacial energy so that the pressure decrease causes the increase of this deficiency owing to less neighbors surrounding the molecules at the surface. The molecular interactions between the dense film of natural gas and water can compensate for the cohesive forces lowering the internal pressure, which leads to lower interfacial energy by the Gibbs equation compared to the pure water liquid-vapor system. Interfacial tension diminution is more highlighted for the natural gas-water system so that it exhibits 17.17-27.26% reduction at P>10 MPa compared to the water-pure methane mixture [54]. Fig. 8 lucidly shows that the computational results are in excellent agreement with the experiments at the different thermodynamic conditions with average absolute deviations (AAD) of 0.19% to 3.35% obtained from [29]:

$$AAD = \frac{1}{N}\sum_{i=1}^{N}\left|\gamma_i - \langle\gamma_{ref}\rangle\right| \times 100 \quad (12)$$

where $\langle\gamma_{ref}\rangle$ and N represent the mean value and the number of references, respectively. The obtained AAD clearly shows the accuracy of using NP_NAT ensemble in MD for a system which involves the interfacial asymmetry. The largest deviation from the experiment is attributed to the system at 1 MPa since MD is slightly instable in low pressure regime (<5 MPa) owing to more pressure fluctuations, particularly in liquid and solid phases. The ADD vanishes as we increase the applied pressure in MD simulations providing more sensible results.

Herein, we systematically increase the system pressure from 1 MPa to 50 MPa at 298.15 K and calculate the interfacial tension to fit the obtained results with a master curve, and subsequently, find a relationship between the interfacial tension and the pressure as given below (units reported in the figure):

$$\gamma = 0.7862\,P - 10.88\,\sqrt{P} + 79.05 \quad (13)$$

(a)

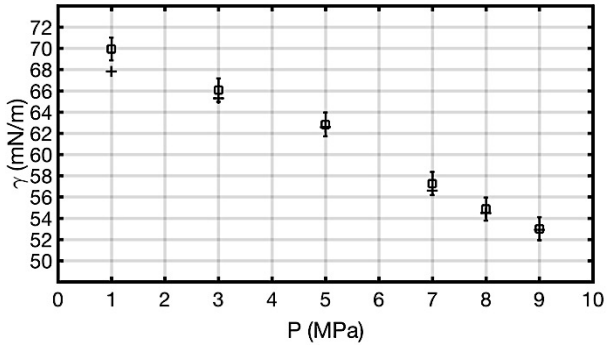

(b)

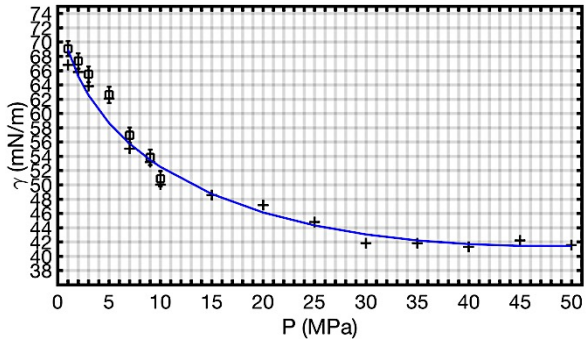

(c)

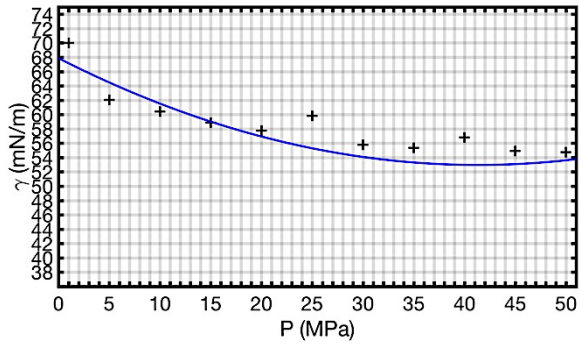

Fig. 8. Interfacial tension (mN/m) of the water-natural gas mixture with increasing the system pressure (MPa) at the temperature of 293.15 K (a) and 298.15 K (b). The plot (c) shows the interfacial tension of the water-pure methane mixture at 298.15 K [54]. The square and plus sign markers represent the data obtained from the experiments by Hayama *et al.* and present work (with blue fitting curve), respectively [29]. The plots explicitly demonstrate that the interfacial tension decreases

when the system is exposed to a pressure upturn, especially in the systems in the lower pressure regime (< 10 MPa).

In comparison with the water-pure methane system, the water-natural gas interfacial tension more rapidly decreases with pressure increase while both systems theoretically have the same interfacial tension of 66.9 mN/m at 298.15 K and 1.66 MPa [54]. Please note that the decrease of the interfacial tension disappears at P>30 MPa, consequently, the interface exhibits a constant tension with pressure upturn up to 50 MPa. This plateau section can be explained by the classic repulsive interactions between the water and nonpolar hydrophobic gas molecules. After the interface is saturated with the natural gas molecules, increasing pressure can no longer change the interfacial thickness, subsequently, the volume and the difference between bulk and interfacial density, which leads to revoking the effect of pressure on the interfacial tension and thickness. Fig. 9 (a) depicts the physical interfacial thickness d(Å) from the density profiles fitted by the hyperbolic tangent functions:

$$\rho(z) = \frac{1}{2}\rho_b \left(1 - \tanh\frac{|z-z_c|-z_G}{d}\right) \quad (14)$$

where ρ_b, z_c, and z_G denote the bulk density (g/cm^3), the center of interface (Å), and the Gibbs dividing surface position (Å), respectively.

In addition to the interfacial thickness, we report the box length in the z dimension (L_z) to evaluate the temperature and the pressure effects on the system. Fig. 9 shows that d (a) and L_z (b) significantly contract or expand to adapt to the new thermodynamic conditions. In summary, the system can reveal large expansion in both d and, more susceptibly, L_z along with temperature rise or pressure drop. Please note that the pressure effect can persist so long as the system continues to hold its conditions which are pertinent to the material compressibility.

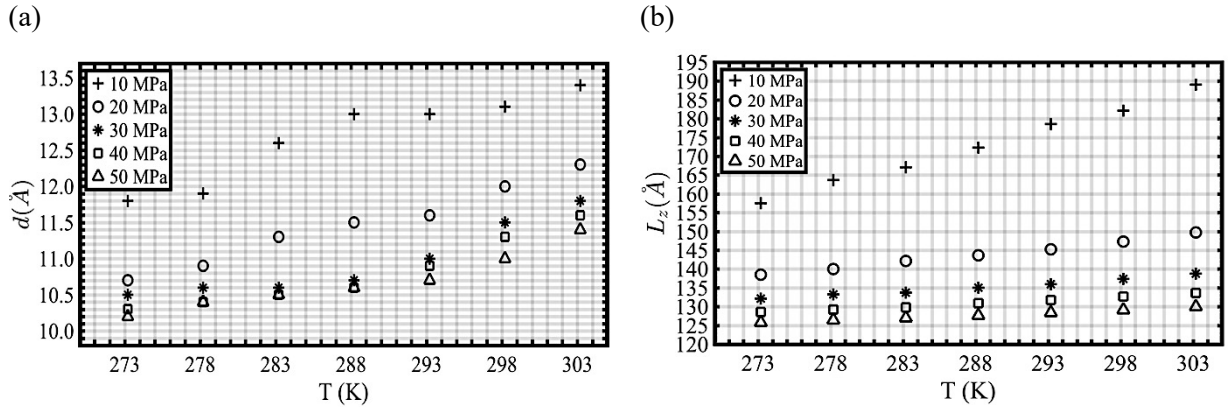

Fig. 9. The temperature upturn triggers an increase in the physical interfacial thickness d (a) and L_z (b) at 10, 20, 30, 40, and 50 MPa represented by plus sign, circle, star, square, and triangle markers, respectively. High temperature regime further manifests the elongation of the box length.

Subsequently, we systematically increase the system temperature in a range of thermodynamically favorable conditions for the hydrate formation and calculate the interfacial tension between the water and gas phases. Fig. 10 shows that the interfacial tension substantially depends on the temperature so that the interfacial tension decreases with increasing temperature, ultimately, the tension vanishes at the critical point. The tension diminution is attributed to the declining cohesive forces acting between the water molecules. In the system with a constant cross-sectional area at 10 MPa, one might fit the interfacial tension values with a quadratic curve in an analogous manner to the interfacial tension-pressure relation (units reported in the figure):

$$\gamma = -0.0001\,T^2 - \ 0.18\,T + 110 \tag{15}$$

Since the second order term is almost negligible, a good linear estimate to the surface tension as shown in Fig. 10 (b) is:

$$\gamma = -0.24\,T + 122.36 \tag{16}$$

Given the considerable adsorbed hydrocarbons acting as surfactants, the interfacial tension is expectedly lower than the surface tension between the pure liquid water in contact with its vapor. Likewise, the natural gas that contains larger hydrocarbons than methane further reduces the tension forasmuch as the fitting line exhibits 4.3% steeper slope in comparison with the mixture of water and pure methane [54].

Moreover, this master curve can correlate the interfacial tension and the temperature with the use of classical scaling laws. The Eötvös rule improved by Ramsay and Shields can perfectly conform by the following formula [60]:

$$\gamma V^{2/3} = k(T_c - T - 6) \quad (17)$$

where V, T_c, and k denote the molar volume, critical temperature of the mixture, and Eötvös constant of 2.1×10^{-7} J/K.mol$^{2/3}$, respectively. Hence, we find that the water-gas mixture with the molar volume of 28.86 cm^3 and the critical temperature of 536.31 K corresponds to the linear fitting line. Interestingly, we can attain very similar molar volume and critical temperature with only 1.9% deviation from the mixing rules providing the system is considered ideal, which again shows the agreement of the simulations with theory [61]. Nevertheless, this linear function may only predict the interfacial tension in the specific range of temperature and pressure since we do not examine the other factors such as molecular orientation, polarity, and structure under different thermodynamic conditions.

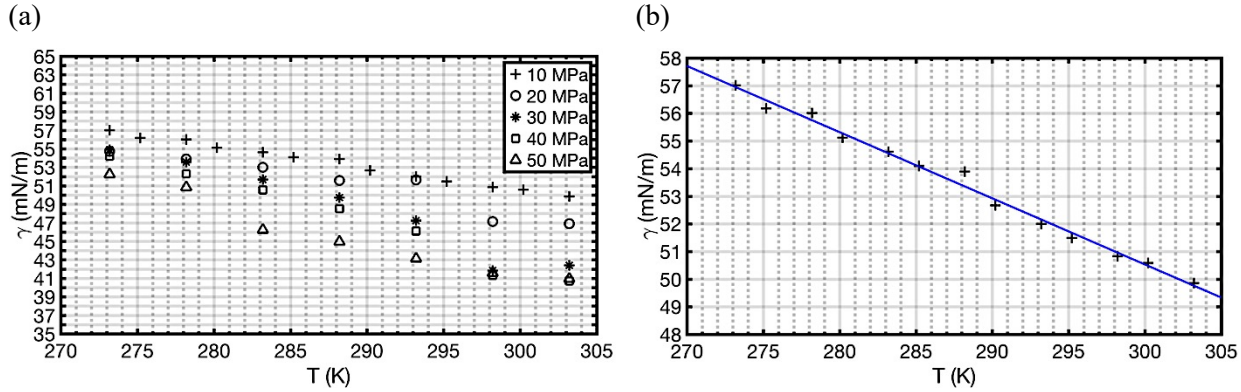

Fig. 10. The plot (a) displays the inverse behavior of the interfacial tension (mN/m) with the temperature (K) upturn at 10 (plus signs), 20 (circles), 30 (stars), 40 (squares), and 50 (triangles) MPa. Blue line in the plot (b) depicts the linear master curves fitting the interfacial tension at 10 MPa. The slope of this line is the surface entropy.

Lastly, we derive the surface entropy (S) from the fundamental thermodynamic equations to find more insights into the effect of temperature on the interfacial tension. We postulate that the surface entropy merely depends on the temperature in a system with relatively constant pressure. One approach is to calculate the surface entropy from the summation of the system enthalpy and the isobaric heat capacity [62]. Here, we propose a more efficient method to derive this surface entropy from the fundamental thermodynamic equations:

$$-S = \left(\frac{\partial G}{\partial T}\right)_{A,P} = \left(\frac{\partial \gamma}{\partial T}\right)_{A,P} \quad (19)$$

For instance, we obtain an entropy value of -133.48 kcal/mol at 298.15 K and 10 MPa, after multiplication by the area and unit conversion. A persistent negative surface entropy in the W/NG mixtures implies that increasing the system temperature must weaken the interfacial tension as a

result of more molecular fluctuation and disorder at the interface, which follows the regular classical behavior with no anomaly, unlike several compounds such as para-azoxyanisole (PAA), p-anisaldazine, and some liquid crystals [63, 64].

Conclusions

In the current study, we employed molecular dynamics simulations to investigate the interfacial thermodynamics, mechanics, and chemical composition at the interface between natural gas and liquid water. We applied a specific NP_NAT ensemble which holds the cross-sectional area and the perpendicular pressure to the planar interface constant owing to the mechanical anisotropy and chemical asymmetry of the water-natural gas interfaces. Both conditions of this ensemble are critical to achieve reliable results in surface studies. The use of such ensemble improved the accuracy of the interfacial properties such as the surface tension, and diminished the deviation between the experiments and computational methods.

The interfacial density profile, surface excess, radial pair distribution function, and chemical compositions in both phases were computed to generate molecular-level characterization. Increasing the interfacial density and excess, and the distribution of the propane, ethane, and methane molecules near the water-gas interface suggests that the surface adsorbs the gas components in order of their size while heavy alkanes reveal lower solubility into the water phase. Priority in the anomalous adsorption of large saturated hydrocarbons such as propane onto the natural gas-water surface implies that the nucleation of structure II clathrates initiated at the interface is recognized as heterogeneous formation in the classical nucleation theory. After a complete enumeration of all hydrogen bonds adjacent to the interface, we speculated that the favorable interactions between the hydrogen bonds in water phase and hydrophobic hydrocarbons in gas phase can elucidate both high adsorption and low solubility of gas molecules, particularly in high pressure regime (P>10 MPa).

The interfacial tension values were calculated and evaluated on the basis of the available experimental data. In conjunction with the computational results, we used the classical scaling laws, for example, the Eötvös rule originated from fundamental thermodynamics to fully characterize the effects of the temperature and pressure on the interfacial properties including the surface tension, thickness, and entropy. We concluded that interfacial tension decreases with an

increase in the system temperature and pressure up to 50 MPa. Given the substantial hydrocarbons adsorption at the interface acting as surfactant, the interfacial tension in a natural gas-water system is more attenuated than the liquid-vapor water or water-pure methane systems at the same temperature and pressure. We employed the adaptive ensemble to capture the elongation of the longitudinal box length and interfacial thickness with either pressure drop or temperature increase.

In summary, these results comprehensively deliver a quantitative and qualitative characterization of the natural gas-water interface which is of great significance to basic surface science and emerging environmental applications.

Acknowledgements

SM appreciates the financial support of the McGill Engineering Doctoral Awards (MEDA) Grad Excellence Award-90025 program. This research is supported by the Natural Sciences and Engineering Research Council (NSERC) RGPAS 446194 & RGPIN 42069-0 through the Discovery Grants Program. We are grateful to Compute Canada and Calcul Québec for the access to HPC facilities and the technical supports. ADR is grateful to McGill University for financial support through the James McGill Professorship appointment.

References

1. Sloan, E.D., *Fundamental principles and applications of natural gas hydrates.* Nature, 2003. **426**(6964): p. 353-363.
2. Khadem, S.A. and R.B. Boozarjomehry, *Development of systematic framework for an intelligent decision support system in gas transmission network.* Industrial & Engineering Chemistry Research, 2015. **54**(43): p. 10768-10786.
3. Haynes, C.A. and R. Gonzalez, *Rethinking biological activation of methane and conversion to liquid fuels.* Nature chemical biology, 2014. **10**(5): p. 331-339.
4. Osborn, S.G., et al., *Methane contamination of drinking water accompanying gas-well drilling and hydraulic fracturing.* proceedings of the National Academy of Sciences, 2011. **108**(20): p. 8172-8176.
5. Harriss, R.C., et al., *Sources of atmospheric methane in the south Florida environment.* Global Biogeochemical Cycles, 1988. **2**(3): p. 231-243.
6. Faramawy, S., T. Zaki, and A.-E. Sakr, *Natural gas origin, composition, and processing: A review.* Journal of Natural Gas Science and Engineering, 2016. **34**: p. 34-54.
7. Khadem, S.A., et al., *Pressure and temperature functionality of paraffin-carbon dioxide interfacial tension using genetic programming and dimension analysis (GPDA) method.* Journal of Natural Gas Science and Engineering, 2014. **20**: p. 407-413.

8. Busch, A. and A. Amann-Hildenbrand, *Predicting capillarity of mudrocks.* Marine and petroleum geology, 2013. **45**: p. 208-223.
9. Nourbakhsh, A., *Determination of capillary pressure, relative permeability and pores size distribution characteristics of coal from Sydney basin-Canada.* 2012.
10. Sloan Jr, E.D. and C. Koh, *Clathrate hydrates of natural gases*. 2007: CRC press.
11. Jendi, Z.M., P. Servio, and A.D. Rey, *Ideal Strength of Methane Hydrate and Ice Ih from First-Principles.* Crystal Growth & Design, 2015. **15**(11): p. 5301-5309.
12. Vlasic, T.M., P. Servio, and A.D. Rey, *Atomistic modeling of structure II gas hydrate mechanics: Compressibility and equations of state.* AIP Advances, 2016. **6**(8): p. 085317.
13. Vlasic, T.M., P.D. Servio, and A.D. Rey, *Effect of Guest Size on the Mechanical Properties and Molecular Structure of Gas Hydrates from First-Principles.* Crystal Growth & Design, 2017. **17**(12): p. 6407-6416.
14. Carroll, J., *Natural gas hydrates: a guide for engineers*. 2014: Gulf Professional Publishing.
15. Koh, C.A., et al., *Fundamentals and applications of gas hydrates.* Annual Review of Chemical and Biomolecular Engineering, 2011. **2**(1): p. 237-257.
16. Knott, B.C., et al., *Homogeneous nucleation of methane hydrates: Unrealistic under realistic conditions.* Journal of the American Chemical Society, 2012. **134**(48): p. 19544-19547.
17. Sarupria, S. and P.G. Debenedetti, *Homogeneous nucleation of methane hydrate in microsecond molecular dynamics simulations.* The journal of physical chemistry letters, 2012. **3**(20): p. 2942-2947.
18. Bai, X.-M. and M. Li, *Test of classical nucleation theory via molecular-dynamics simulation.* The Journal of chemical physics, 2005. **122**(22): p. 224510.
19. Lupi, L., B. Peters, and V. Molinero, *Pre-ordering of interfacial water in the pathway of heterogeneous ice nucleation does not lead to a two-step crystallization mechanism.* The Journal of Chemical Physics, 2016. **145**(21): p. 211910.
20. Warrier, P., et al., *Overview: Nucleation of clathrate hydrates.* The Journal of Chemical Physics, 2016. **145**(21): p. 211705.
21. Kashchiev, D. and A. Firoozabadi, *Nucleation of gas hydrates.* Journal of Crystal Growth, 2002. **243**(3–4): p. 476-489.
22. Kashchiev, D., *Nucleation : basic theory with applications*. 2000, Butterworth Heinemann: Oxford.
23. Bagherzadeh, S.A., et al., *Influence of hydrated silica surfaces on interfacial water in the presence of clathrate hydrate forming gases.* The Journal of Physical Chemistry C, 2012. **116**(47): p. 24907-24915.
24. Bai, D., et al., *How properties of solid surfaces modulate the nucleation of gas hydrate.* Scientific reports, 2015. **5**: p. 12747.
25. Liang, S. and P.G. Kusalik, *The nucleation of gas hydrates near silica surfaces.* Canadian Journal of Chemistry, 2014. **93**(8): p. 791-798.
26. Aman, Z.M. and C.A. Koh, *Interfacial phenomena in gas hydrate systems.* Chemical Society Reviews, 2016. **45**(6): p. 1678-1690.
27. Grimvall, G., *Chapter 6 - The phonon spectrum*, in *Thermophysical Properties of Materials*. 1999, Elsevier Science B.V.: Amsterdam. p. 79-111.
28. Kashchiev, D. and A. Firoozabadi, *Induction time in crystallization of gas hydrates.* Journal of crystal growth, 2003. **250**(3-4): p. 499-515.

29. Hayama, H., et al., *Interfacial tension between (methane+ ethane+ propane) gas mixture and water from 283.2 K to 298.2 K under up to 10 MPa.* The Journal of Chemical Thermodynamics, 2017. **108**: p. 71-75.
30. Speight, J.G., *Chapter 5 - Properties of Organic Compounds*, in *Environmental Organic Chemistry for Engineers*, J.G. Speight, Editor. 2017, Butterworth-Heinemann. p. 203-261.
31. Wang, L.-K., et al., *Experimental study on the solubility of natural gas components in water with or without hydrate inhibitor.* Fluid Phase Equilibria, 2003. **207**(1-2): p. 143-154.
32. Demirbas, A., *Methane gas hydrate*. 2010: Springer Science & Business Media.
33. Klauda, J.B. and S.I. Sandler, *Global distribution of methane hydrate in ocean sediment.* Energy & Fuels, 2005. **19**(2): p. 459-470.
34. Binks, B.P. and J.H. Clint, *Solid wettability from surface energy components: relevance to pickering emulsions.* Langmuir, 2002. **18**(4): p. 1270-1273.
35. Vázquez, U.O.M., et al., *Calculating the surface tension between a flat solid and a liquid: a theoretical and computer simulation study of three topologically different methods.* Journal of Mathematical Chemistry, 2009. **45**(1): p. 161-174.
36. Chaplin, M., *Theory vs experiment: what is the surface charge of water?* Water Journal Multidisciplinary Research Journal 1, 2009: p. 1-28.
37. Eisenberg, D., D.S. Eisenberg, and W. Kauzmann, *The structure and properties of water*. 2005: Oxford University Press on Demand.
38. Biscay, F., et al., *Monte Carlo simulations of the pressure dependence of the water− acid gas interfacial tensions.* The Journal of Physical Chemistry B, 2009. **113**(43): p. 14277-14290.
39. Biscay, F., et al., *Monte Carlo calculation of the methane-water interfacial tension at high pressures.* The Journal of chemical physics, 2009. **131**(12): p. 124707.
40. Noya, E.G., C. Vega, and E. de Miguel, *Determination of the melting point of hard spheres from direct coexistence simulation methods.* The Journal of chemical physics, 2008. **128**(15): p. 154507.
41. Ikeguchi, M., *Partial rigid-body dynamics in NPT, NPAT and NPγT ensembles for proteins and membranes.* Journal of computational chemistry, 2004. **25**(4): p. 529-541.
42. Kvamme, B., T. Kuznetsova, and K. Schmidt. *Experimental measurements and numerical modelling of interfacial tension in water-methane systems*. in *Presentation at the International Conference of Computational Methods in Sciences and Engineering, Chania, Greece*. 2006.
43. Schmidt, K.A., G.K. Folas, and B. Kvamme, *Calculation of the interfacial tension of the methane–water system with the linear gradient theory.* Fluid Phase Equilibria, 2007. **261**(1): p. 230-237.
44. Kirkwood, J.G. and F.P. Buff, *The statistical mechanical theory of surface tension.* The Journal of Chemical Physics, 1949. **17**(3): p. 338-343.
45. Ghoufi, A. and P. Malfreyt, *Calculation of the surface tension and pressure components from a non-exponential perturbation method of the thermodynamic route.* The Journal of chemical physics, 2012. **136**(2): p. 024104.
46. Tolman, R.C., *Consideration of the Gibbs theory of surface tension.* The journal of chemical physics, 1948. **16**(8): p. 758-774.

47. Ghadar, Y. and A.E. Clark, *Intermolecular network analysis of the liquid and vapor interfaces of pentane and water: microsolvation does not trend with interfacial properties.* Physical Chemistry Chemical Physics, 2014. **16**(24): p. 12475-12487.
48. Horn, H.W., et al., *Development of an improved four-site water model for biomolecular simulations: TIP4P-Ew.* The Journal of chemical physics, 2004. **120**(20): p. 9665-9678.
49. Jorgensen, W.L., J.D. Madura, and C.J. Swenson, *Optimized intermolecular potential functions for liquid hydrocarbons.* Journal of the American Chemical Society, 1984. **106**(22): p. 6638-6646.
50. Plimpton, S., *Fast parallel algorithms for short-range molecular dynamics.* Journal of computational physics, 1995. **117**(1): p. 1-19.
51. Hockney, R.W. and J.W. Eastwood, *Computer simulation using particles*. 1988: crc Press.
52. Isele-Holder, R.E., W. Mitchell, and A.E. Ismail, *Development and application of a particle-particle particle-mesh Ewald method for dispersion interactions.* The Journal of chemical physics, 2012. **137**(17): p. 174107.
53. Rowlinson, J.S. and B. Widom, *Molecular theory of capillarity*. 2013: Courier Corporation.
54. Mirzaeifard, S., P. Servio, and A.D. Rey, *Molecular dynamics characterization of temperature and pressure effects on the water-methane interface.* Colloid and Interface Science Communications, 2018. **24**: p. 75-81.
55. Blokhuis, E., et al., *Tail corrections to the surface tension of a Lennard-Jones liquid-vapour interface.* Molecular Physics, 1995. **85**(3): p. 665-669.
56. Chapela, G.A., et al., *Computer simulation of a gas–liquid surface. Part 1.* Journal of the Chemical Society, Faraday Transactions 2: Molecular and Chemical Physics, 1977. **73**(7): p. 1133-1144.
57. Grest, G.S., et al., *Substructured multibody molecular dynamics*. 2006, Sandia National Laboratories.
58. Sakamaki, R., et al., *Thermodynamic properties of methane/water interface predicted by molecular dynamics simulations.* The Journal of chemical physics, 2011. **134**(14): p. 144702.
59. Scharlin, P., et al., *Solubility of gases in water: Correlation between solubility and the number of water molecules in the first solvation shell.* Pure and applied chemistry, 1998. **70**(10): p. 1895-1904.
60. Udeagbara, S.G., *Effect of Temperature and Impurities on Surface Tension of Crude Oil*. 2010: Universal-Publishers.
61. McCain, W.D., *The properties of petroleum fluids*. 1990: PennWell Books.
62. Jacobson, L.C., W. Hujo, and V. Molinero, *Thermodynamic stability and growth of guest-free clathrate hydrates: a low-density crystal phase of water.* The Journal of Physical Chemistry B, 2009. **113**(30): p. 10298-10307.
63. Chandrasekhar, S., *Liquid Crystals*. 2nd ed. 1992: Cambridge University Press. p. 80-84.
64. Rey, A.D., *Modeling the Wilhelmy surface tension method for nematic liquid crystals.* Langmuir, 2000. **16**(2): p. 845-849.